JOURNAL OF MATERIALS SCIENCE 21 (1986) 4250–4256

The microstructure of WC and WC–4.3 wt% Co sintered at high pressure

YUSUKE MORIYOSHI, MINORU AKAISHI, OSAMU FUKUNAGA
National Institute for Research in Inorganic Materials, 1-1 Namiki, Sakura-mura, Niiharigun, Ibaraki 305, Japan

WC and WC–4.3 wt% Co were sintered at 1400° C under the condition of 5.8 GPa by using a modified belt-type high pressure apparatus. Their microstructures were observed with a transmission electron microscope, in order to clarify the structural features and sintering mechanisms of the materials. As a result, a stacking-fault vector and mobile dislocations during sintering were determined. Also, it is concluded that the sintering mechanisms of WC and WC–4.3 wt% Co are plastic deformation and solution precipitation through the liquid binder phase, respectively.

1. Introduction

Non-oxide materials such as diamond, Si_3N_4, B_4C, SiC, WC, etc. are difficult to sinter to high density under normal sintering conditions, because of the very small diffusion coefficients of ions in these materials. Therefore, in order to enhance the sinterability, hot pressing, hot isostatic pressing and high-pressure sintering have been successfully considered to obtain a sintered body with high density.

Among the above sintering methods, hot pressing and hot isostatic pressing are particularly popular as sintering methods. High-pressure sintering is not so popular, but has been used more in attempts to sinter non-sinterable materials. Many workers have tried to sinter non-sinterable materials at high pressure. For instance, Hall [1], Stromberg and Stephens [2] and Suzuki *et al.* [3] have sintered a diamond without additives. Katzman and Libby [4], Wentorf and Rocco [5, 6], Notsu *et al.* [7], and Akashi *et al.* [8] have sintered a diamond in the presence of cobalt. High-pressure sintering retards grain growth and enhances densification, and as a result a sintering body with high strength can be obtained.

High-pressure sintering of WC has been performed by Kudaka *et al.* [9], but the sample obtained was too small to measure the density. Also, high-pressure sintering of TaC has been performed by Yohe and Rouff [10]. We previously carried out high-pressure sintering of WC and WC–4.3 wt % Co with a belt-type high pressure apparatus [11], and indicated that the maximum hardness and relative density of WC under the conditions of 5.8 GPa and 1400 to 1500° C were 2550 kg mm^{-2} and 96%, respectively. At the time, the structural features of the materials were not studied; therefore, in this paper we intend to describe the microstructural features of both WC and WC–4.3 wt % Co sintered at 5.8 GPa and 1400° C, particularly to clarify the sintering mechanisms of the materials from the microstructural data.

2. Experimental procedure

Commercially available WC (A-WC) and WC–4.3 wt % Co (b-WC) were used as starting samples in this experiment. Analytical data for both samples are listed in Table I. The impurities of 5 to 30 p.p.m. Fe, Ni and Co were detected in A-WC by a spark-source mass spectrograph. The particle size of these samples is about 0.5 μm as shown in Fig. 1. Sintering was carried out at 1400° C under 5.8 GPa by using a modified belt-type high-pressure apparatus with 25 mm bore diameter which has been reported previously [11].

The assembly shown in Fig. 2 was used. Fig. 2a is a full illustration, and Fig. 2b is an enlarged portion around the WC powder. The sample, as shown in Fig. 2b, was wrapped with zirconium foil and surrounded by sodium chloride. Sodium chloride has a very low shear strength at both room and high temperatures. It envelops the sample under an effectively hydrostatic condition. Pressure correction at room temperature was made on the basis of the electrical conductivity of bismuth (2.54 GPa), thallium (3.6 GPa) and barium (5.5 GPa). Pressure correction at high temperature was based on the solubility curve of silver determined with a piston cylinder-type high-pressure apparatus. The effect of pressure on the thermoelectromotive force of the thermocouple was not corrected in this experiment. Considering these electrical conductivity data, we chose the condition of 1400° C at 5.8 GPa for sintering. The sample was pressed under the pressure of 5.8 GPa at room temperature. It was then heated at a constant rate of 50° C min^{-1}. At the given temperature the sample was maintained for 30 min and then cooled to room temperature in about 40 min. After the sample was cooling, the pressure was slowly released in order to minimize the residual strains. The density of sintered

TABLE I Cobalt and carbon contents of starting materials

Material	Cobalt (wt %)	Total carbon (wt %)	Free carbon (wt %)
A-WC	0	6.16	0.04
B-WC	4.31	6.02	0.15

0022–2461/86 $03.00 + .12

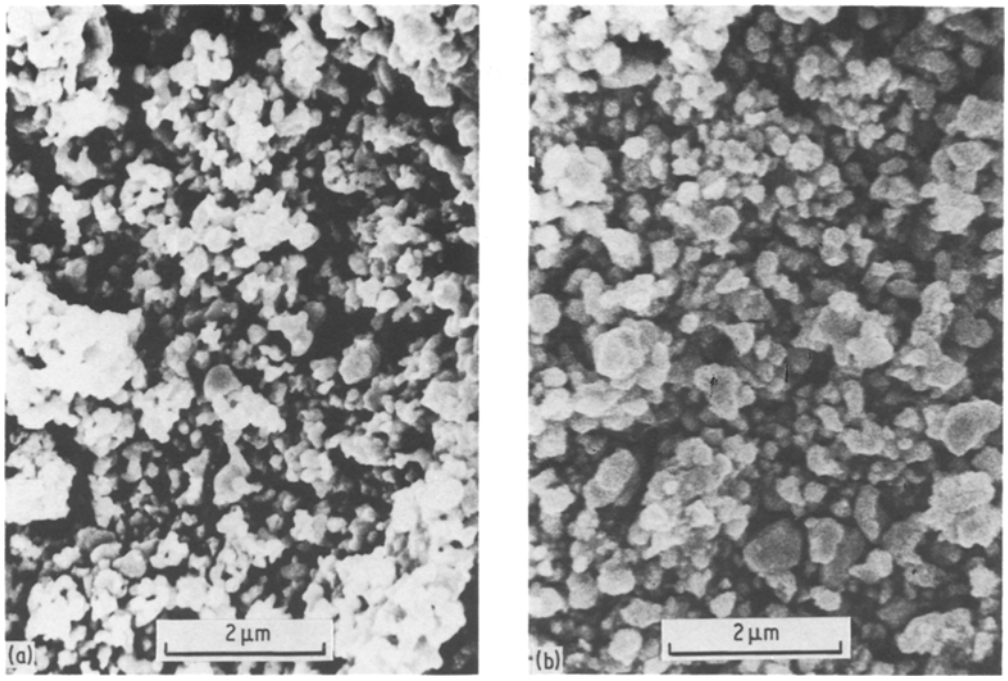

Figure 1 SEM micrographs of (a) WC and (b) WC–4.3 wt % Co powder.

bodies of both A-WC and B-WC was about 96% of theoretical.

The sintered body was firstly cut to a thin plate with a diamond wheel; thereafter it was ground on a diamond disc to a plate as thin as 150 μm. Finally it was ion-thinned and observed with a 1000 kV transmission electron microscope (TEM). Also, the fracture surface of a sintered body was observed with a scanning electron microscope (SEM).

3. Experimental results

Fig. 3 shows SEM micrographs of the fracture surfaces of sintered bodies of both A-WC and B-WC. It is clear from the figure that grain growth takes place in B-WC but no grain growth in A-WC.

Fig. 4 shows typical microstructures of A-WC. As can be seen in the figure, we can see dark contrast which indicates structural defects such as stacking faults, dislocations and glide planes. The concentration of defects is so high that a boundary between two grains cannot be observed. From Fig. 5 we can clearly see glide planes which are parallel to the $\langle 0\,0\,0\,1 \rangle$ direction. This is due to plastic deformation by the motion of dislocations with Burgers vector $\boldsymbol{b} = \langle 0\,0\,0\,1 \rangle$. Dislocations with another Burgers vector would be also movable as mentioned later. Fig. 6 shows a crack between two grains as shown by an arrow. These results indicate that very active plastic deformation takes place during sintering. The defect concentration is too high to see WC grains in the sintered bodies. WC grains can be detected by selected-area electron diffraction pattern as shown in the inset to Fig. 6.

Fig. 7 shows the typical microstructure of B-WC. As can be seen in the figure, we can clearly identify WC grains. The concentration of structural defects such as stacking faults, dislocations and glide planes is smaller than in A-WC. This would be related to the effects of cobalt on stress relaxation during sintering. However, since the cobalt content is relatively small, X-ray diffraction patterns show no diffraction peaks of cobalt except those of WC. Under these sintering conditions, WC would form a solid solution with cobalt. The eutectic point of the WC–Co system is lower than the sintering temperature, so that the binder phase is a liquid which allows stress relaxation in the high-pressure sintering. The binder phase can be detected by selected-area electron diffraction patterns at three-grain junctions. A neck between two grains generally has no curvature but it is angular.

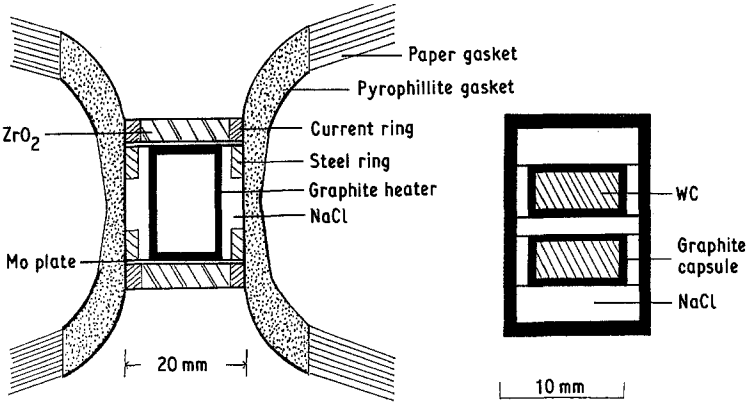

Figure 2 Sample assembly for high-pressure sintering. (a) Full illustration, (b) enlarged portion around the sample.

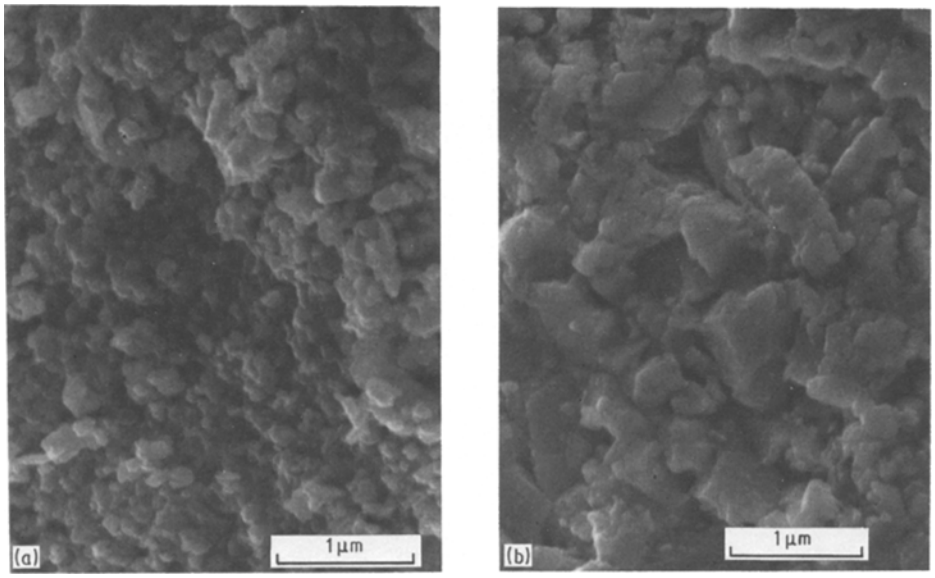

Figure 3 SEM micrographs of (a) WC and (b) WC–4.3 wt % Co.

Fig. 8 shows stacking faults and dislocations in a grain in B-WC. Fig. 9 shows stacking faults for various diffraction vectors. Stacking faults are visible for diffraction vectors $\boldsymbol{g} = [0\,\bar{1}\,1\,\bar{2}]$, $[\bar{2}\,2\,0\,\bar{2}]$ and $[\bar{1}\,0\,1\,0]$; on the other hand, they are out of contrast for diffraction vectors $\boldsymbol{g} = [2\,\bar{1}\,\bar{1}\,0]$, $[1\,\bar{2}\,1\,2]$ and $[4\,2\,\bar{2}\,2]$. The stacking faults are out of contrast when the phase vector $2\pi\boldsymbol{R}\cdot\boldsymbol{g}$ is an integer times 2π, where $\boldsymbol{R}$ is a fault vector. The present data calculated for various values of $\boldsymbol{g}$ obtained here, together with the phase vectors in hexagonal crystals, are listed in Table II. As can be seen in the table, our data satisfy

TABLE II Phase factors* for various values of $\boldsymbol{g}$ and $\boldsymbol{R}$

$\boldsymbol{g}$	$\boldsymbol{R}$			
	$\frac{1}{2}\boldsymbol{C}+\boldsymbol{P}$	$\frac{1}{2}\boldsymbol{C}+\frac{1}{2}\boldsymbol{a}$		
	$\frac{1}{6}\langle 20\bar{2}3\rangle$	$\frac{1}{6}[2\,\bar{1}\,\bar{1}\,3]$	$\frac{1}{6}[\bar{1}\,2\,\bar{1}\,3]$	$\frac{1}{6}[\bar{1}\,\bar{1}\,2\,3]$
$0\,\bar{1}\,1\,\bar{2}$	$\frac{2}{3}\pi$	0	π	π
$\bar{2}\,2\,0\,\bar{2}$	$\frac{1}{3}\pi$	0	0	0
$\bar{1}\,0\,1\,0$	$\frac{1}{3}\pi$	π	0	π
$2\,\bar{1}\,\bar{1}\,0$	0	0	π	π
$1\,\bar{2}\,1\,2$	0	π	0	π
$4\,\bar{2}\,\bar{2}\,2$	0	0	0	0

*$\boldsymbol{a} = \frac{1}{3}\langle 2\,\bar{1}\,\bar{1}\,0\rangle$, $\boldsymbol{P} = \frac{1}{3}\langle 10\,\bar{1}\,0\rangle$, $\boldsymbol{C} = [0\,0\,0\,1]$.

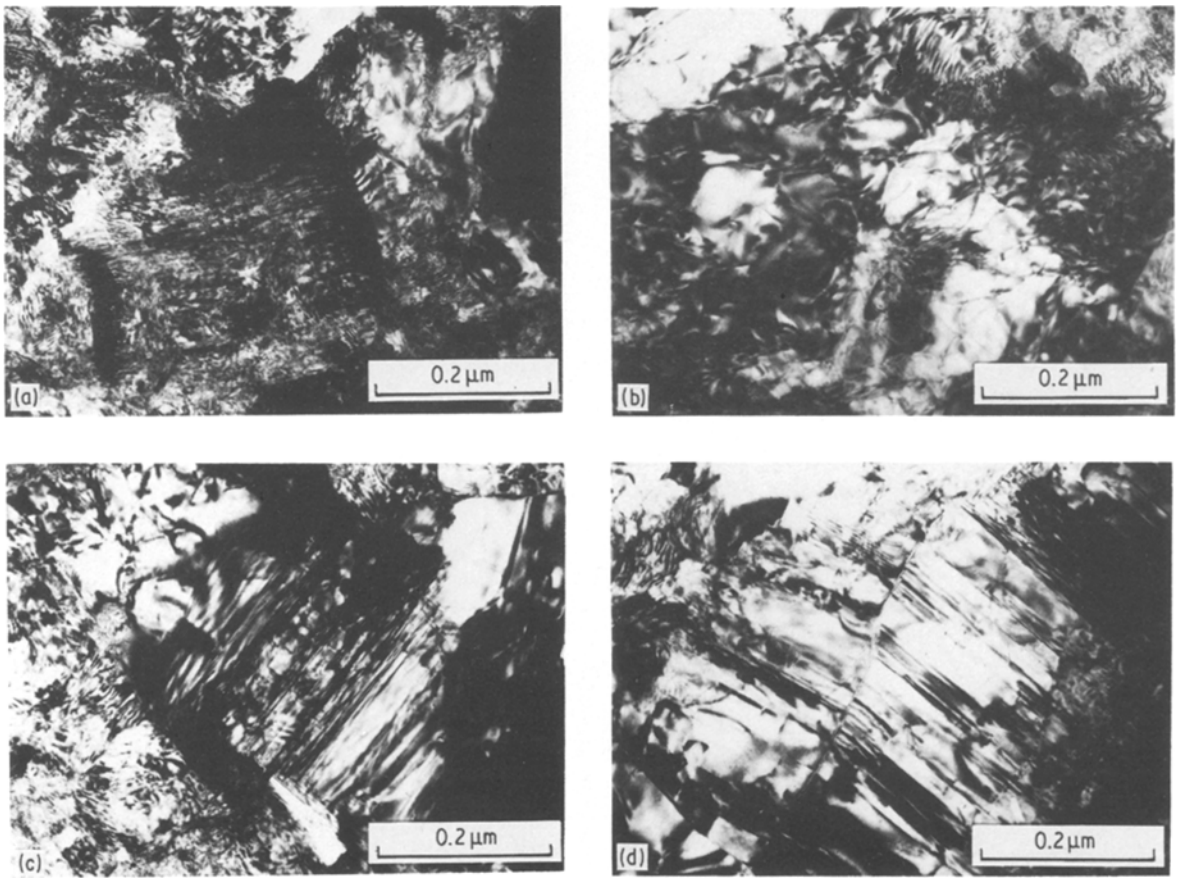

Figure 4 (a–d) TEM micrographs of WC.

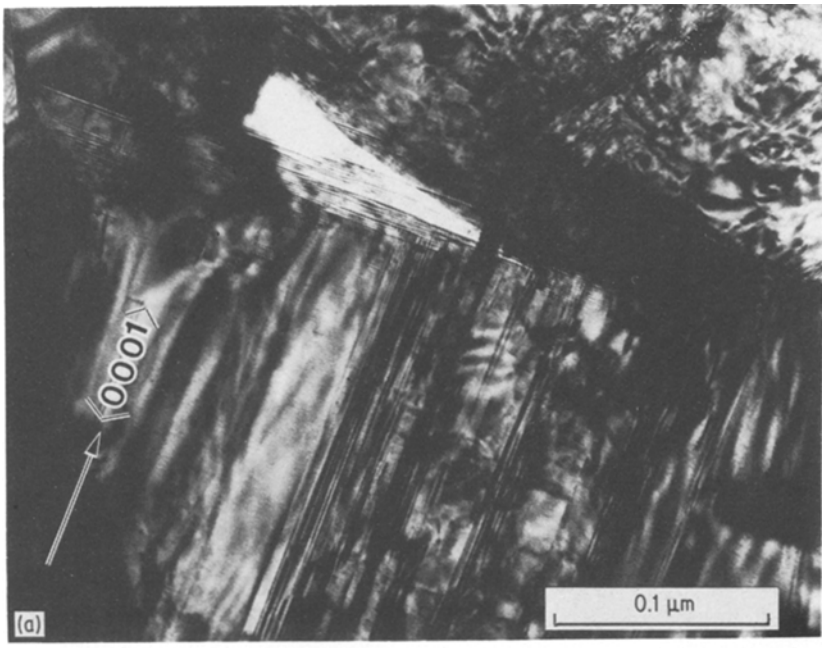

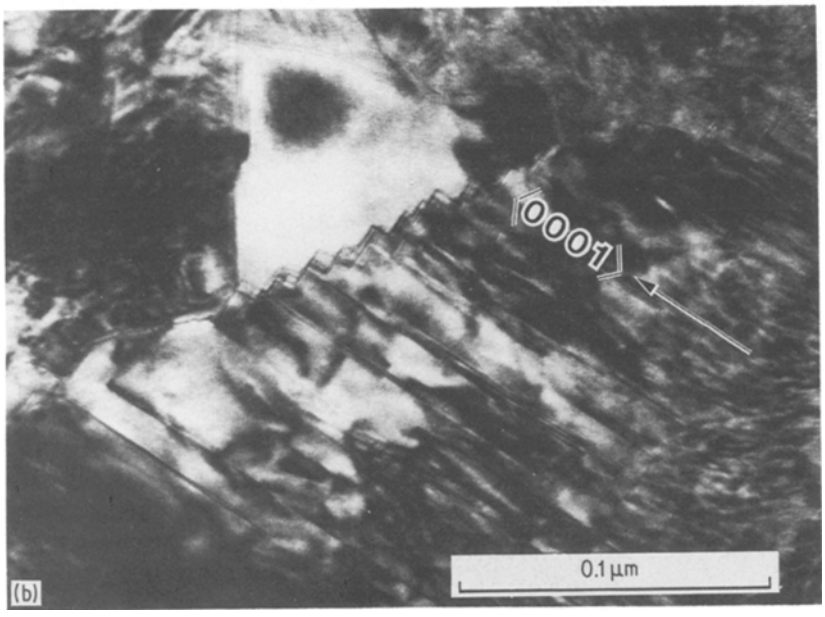

Figure 5 (a, b) TEM micrographs of WC. Glide planes can be seen.

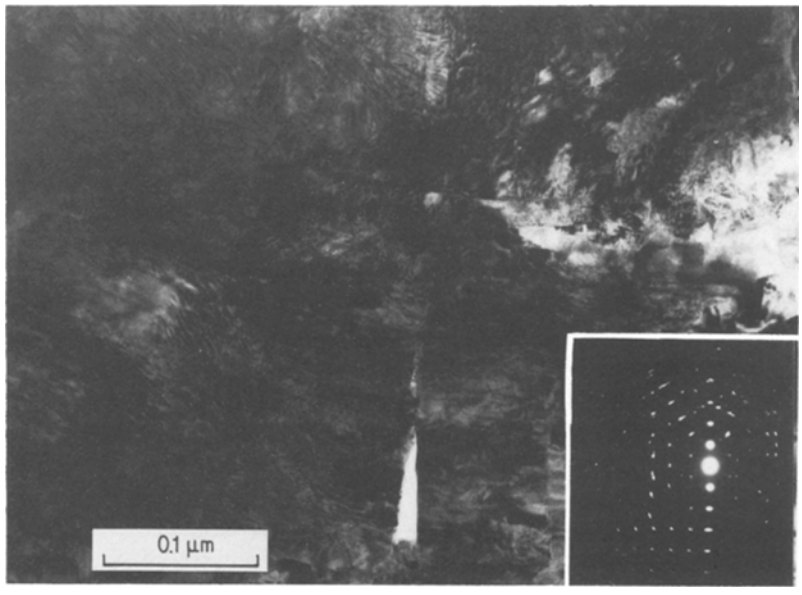

Figure 6 TEM micrograph of WC.

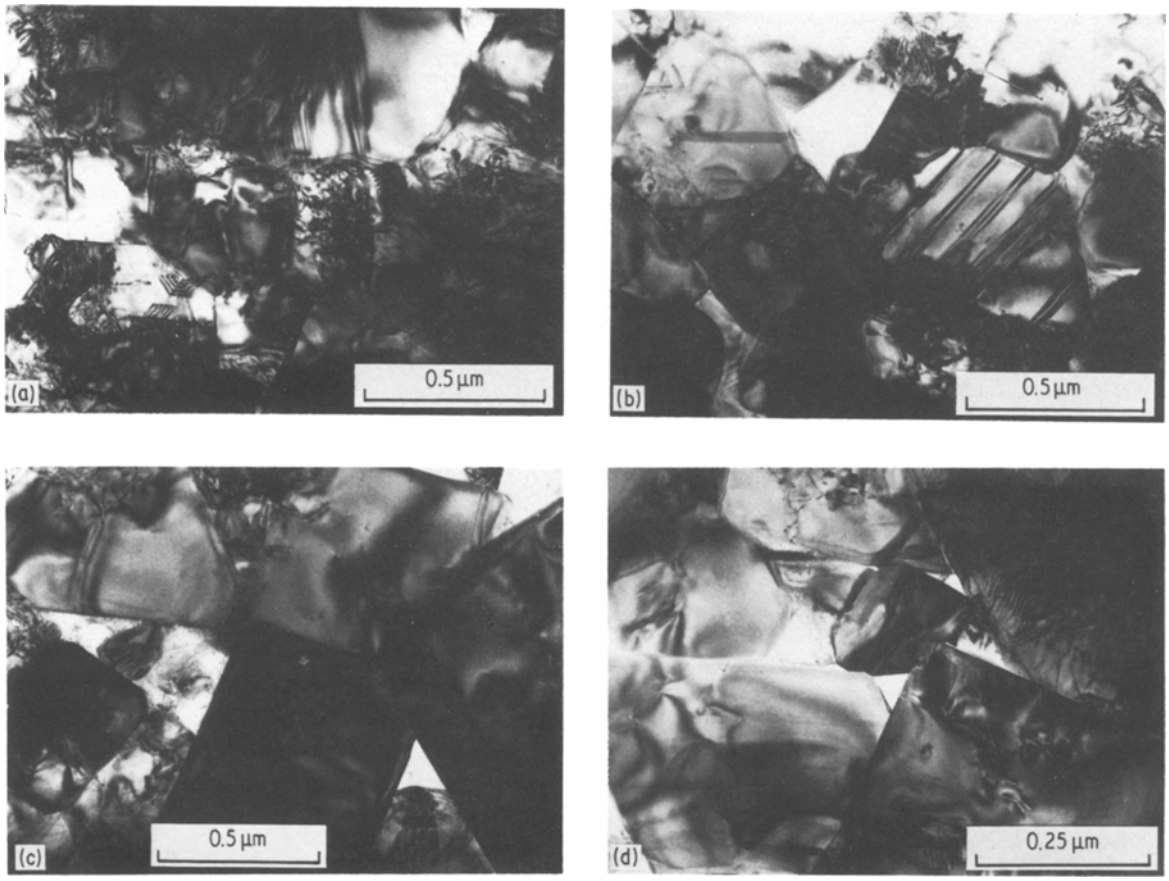

Figure 7 (a–d) TEM micrographs of WC–4.3 wt % Co.

$\boldsymbol{R} = \frac{1}{2}\boldsymbol{a} + \boldsymbol{P}$, where $\boldsymbol{a} = \frac{1}{3}\langle 2\bar{1}\bar{1}0\rangle$, $\boldsymbol{c} = [0001]$ and $\boldsymbol{P} = \frac{1}{3}\langle 10\bar{1}0\rangle$.

4. Discussion

As mentioned before, there are dislocations with Burgers vectors such as $\langle 0001\rangle$, $\frac{1}{3}\langle 11\bar{2}3\rangle$, $\frac{1}{3}\langle 2\bar{1}\bar{1}0\rangle$ and $\frac{1}{3}\langle\bar{2}113\rangle$ in WC. As the energy per unit length of a dislocation is proportional to $\boldsymbol{b}^2$, the energies of dislocations with Burgers vector $\langle 0001\rangle$, $\frac{1}{3}\langle 11\bar{2}3\rangle$, $\frac{1}{3}\langle 2\bar{1}\bar{1}0\rangle$ and $\frac{1}{3}\langle\bar{2}113\rangle$ are proportional to $0.96\boldsymbol{a}^2$, $1.94\boldsymbol{a}^2$, $\boldsymbol{a}^2$ and $1.94\boldsymbol{a}^2$, respectively. Therefore, the dislocation motions of $\boldsymbol{b} = \frac{1}{3}\langle 11\bar{2}3\rangle$ and $\frac{1}{3}\langle\bar{2}113\rangle$ are more difficult than those of $\langle 0001\rangle$ and $\frac{1}{3}\langle 2\bar{1}\bar{1}0\rangle$. However, these have the possibility of an energy decrease from $1.94\boldsymbol{a}^2$ to $0.57\boldsymbol{a}^2 + 0.57\boldsymbol{a}^2$ by the following reactions [12]:

$$\frac{1}{3}\langle 11\bar{2}3\rangle = \frac{1}{6}\langle 20\bar{2}3\rangle + \frac{1}{6}\langle 02\bar{2}3\rangle$$

$$\frac{1}{3}\langle\bar{2}113\rangle = \frac{1}{6}\langle\bar{2}023\rangle + \frac{1}{6}\langle\bar{2}203\rangle$$

These results indicate the possibility that all the dislocations with the above Burgers vectors would be able to move under a stress; that is, the sintering of A-WC takes place by plastic deformation.

The hardness of sintered A-WC is 2550 kg mm^{-2}. This is the same value as the maximum for a (0001) surface in single-crystal WC. The high hardness value of sintered A-WC may be related to the high dislocation

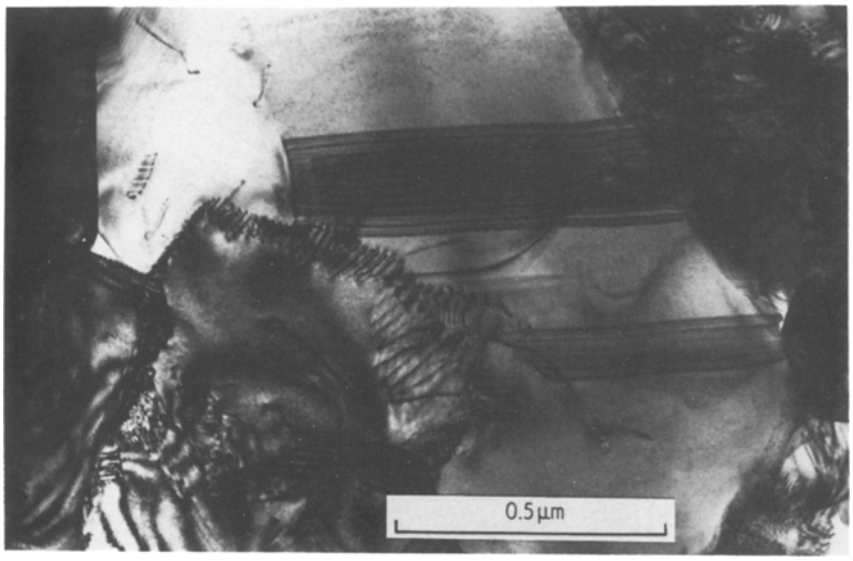

Figure 8 Stacking faults and dislocations in WC–4.3 wt % Co.

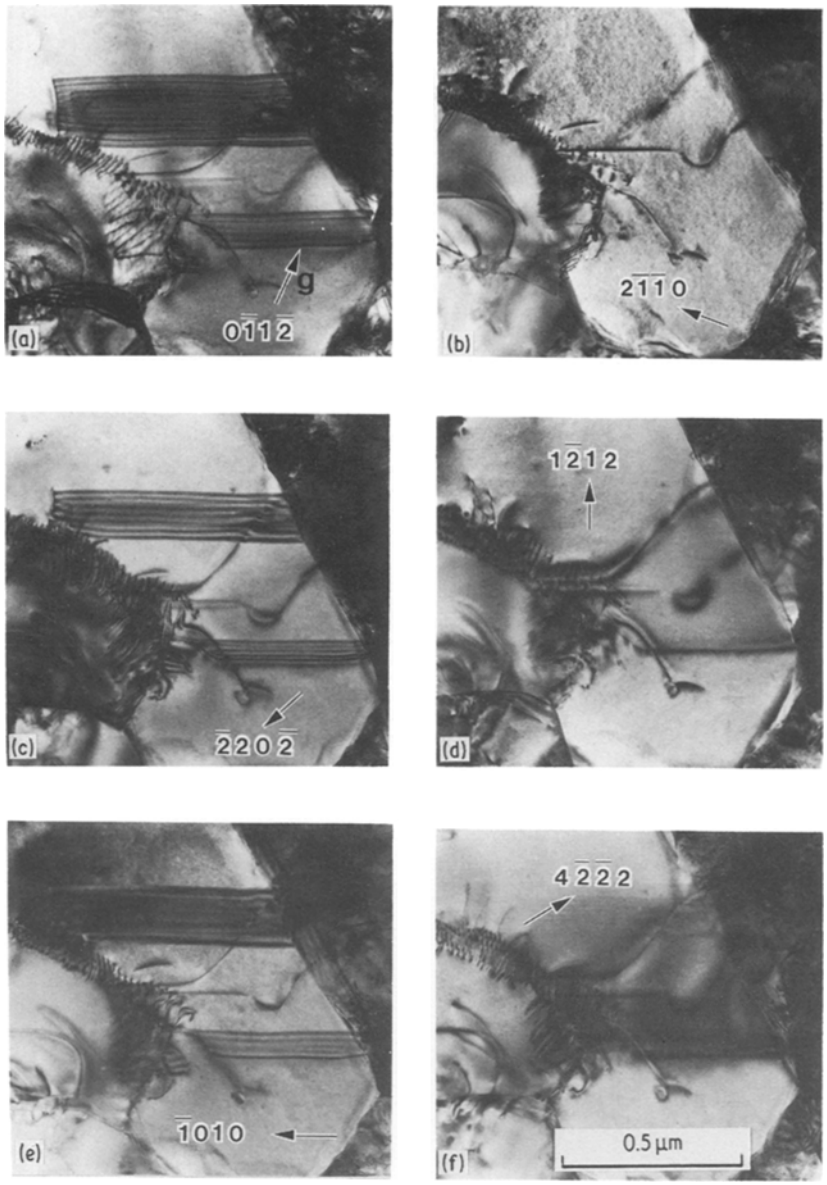

Figure 9 (a–f) stacking faults for various diffraction conditions.

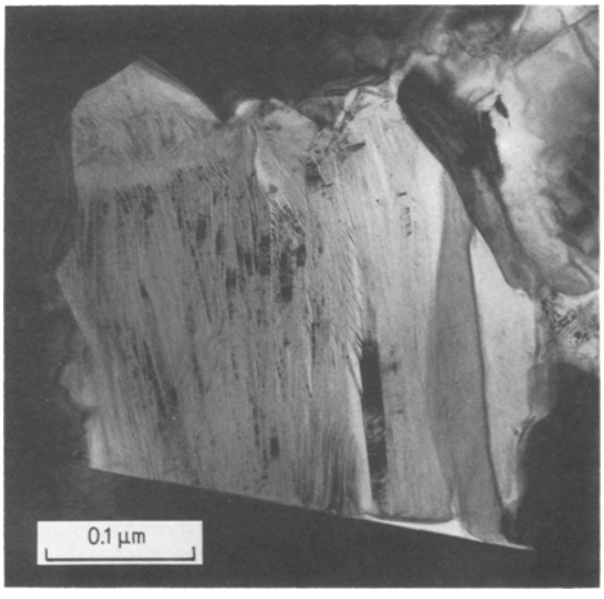

Figure 10 Lamellae of hcp type in the binder phase.

density, since the strain fields of dislocations begin to interact with each other and it becomes more difficult for the dislocations to glide.

As mentioned before, grain growth takes place in B-WC in which WC grains generally have a crystal habit, also a neck between two grains is angular. The reason for this is that the sintering is B-WC takes place by solution–precipitation, the so-called Ostwald ripening [13], of WC atoms through the liquid phase. In this process, WC atoms on a surface with a high surface energy would diffuse to a surface with a relatively lower surface energy, and not to a neck between two grains. The average hardness measured was 1820 kg mm^{-2}, which is smaller than that of A-WC. The smaller hardness would be due to the existence of the binder phase. Lamellae of hcp type formed in the binder phase on deformation are sometime found in B-WC, as shown in Fig. 10. The mechanisms of lamella formation during high-pressure sintering were discussed in detail by Sarin and Johannesson [14].

References

1. H. T. HALL, *Science* **169** (1970) 868.
2. H. D. STROMBERG and D. R. STEPHENS, *Ceram. Bull.* **49** (1970) 1030.
3. N. SUZUKI, A. NAKAUE and O. OKUMA, *J. Jpn High Press.* **11** (1974) 301.
4. H. KATZMAN and W. F. LIBBY, *Science* **172** (1971) 1132.
5. R. H. WENTORF Jr and W. A. ROCCO, US Patent 3 745 623 (1973).
6. *Idem*, US Patent 3 767 371 (1973).
7. Y. NOTSU, T. NAKAJIMA and N. KAWAI, *Mater. Res. Bull.* **12** (1977) 1079.
8. M. AKAISHI, H. KANDA, Y. SATO, N. SETAKA, T. OHSAWA and O. FUKUNAGA, *J. Mater. Sci.* **17** (1982) 193.
9. K. KUDAKA, H. KONNO and T. MATOBA, *Trans. JIM* **31** (1967) 177.
10. W. C. YOHE and A. L. RUOFF, *Amer. Ceram. Soc. Bull.* **57** (1978) 1123.
11. O. FUKUNAGA, S. YAMAOKA, T. ENDOH, M. AKAISHI and H. KANDA, in Proceedings of 6th AIRAPT Conference on High Pressure Science and Technology, July 1977, Boulder, Colorado, Vol. 1, edited by K. D. Timmerhaus and M. S. Barber (Plenum, New York, 1979) p. 864.
12. J. D. BOLTON and M. REDINGYON, *J. Mater. Sci.* **15** (1980) 3150.
13. R. D. VENGRENOVITCH, *Acta Metall.* **30** (1982) 1079.
14. V. K. SARIN and T. JOHANNESSON, *Metal. Sci.* **9** (1975) 472.

Received 14 January
and accepted 13 March 1986